

Highlights

Hydro-morphodynamics 2D modelling using a discontinuous Galerkin discretisation

Mariana C. A. Clare, James R. Percival, Athanasios Angeloudis, Colin J. Cotter, Matthew D. Piggott

- Implementation of a new morphodynamic model within a code generating framework
- Novel use of discontinuous Galerkin based finite element methods to solve this system
- Model simulates suspended and bedload transport with gravity and helical flow effects
- Successful validation evidence through standard trench migration and meander cases

Hydro-morphodynamics 2D modelling using a discontinuous Galerkin discretisation

Mariana C. A. Clare^{a,*}, James R. Percival^a, Athanasios Angeloudis^b, Colin J. Cotter^c and Matthew D. Piggott^a

^aDepartment of Earth Science and Engineering, Imperial College London, UK.

^bSchool of Engineering, Institute for Infrastructure & Environment, University of Edinburgh, UK.

^cDepartment of Mathematics, Imperial College London, UK.

1. Introduction

Data from 2010 shows that almost 400 million people lived in areas less than 5m above average sea level (CIESIN, 2013) and this population keeps growing. As sea levels rise and with the potential for storms to increase in strength and frequency due to a changing climate, the coastal zone is becoming an ever more critical location for the application of advanced modelling techniques. A significant example is the development and application of improved morphodynamic models to simulate sediment transport accurately. The effects of climate change will cause hydrodynamic changes leading to increased erosion risk in coastal zones. The coupled and non-linear nature of this problem makes it especially challenging, since models must solve both hydrodynamic and sediment transport processes together with their two-way coupled interactions. Furthermore, there are two types of sediment transport processes that should be resolved: suspended sediment in the fluid and bedload transport propagating along the bed itself.


Over the last 40 years, increasingly sophisticated morphodynamic models have been developed to predict sediment transport in fluvial and coastal zones. These models can be one-dimensional (1D), two-dimensional (2D) or three-dimensional (3D), and are discussed in detail in Amoudry (2008), Amoudry and Souza (2011) and Papanicolaou et al. (2008), which we draw upon for a brief review here. 1D models generally use finite difference methods to solve a simple system of equations and are the cheapest computationally. However, they cannot capture velocity in the cross-stream and vertical directions. 2D (or 2DH) models adopt the shallow water approximation and can use finite difference (e.g. XBeach – Roelvink et al., 2015), finite volume (e.g. Mike 21 – Warren and Bach, 1992), or finite element based methods to solve a more complex system of equations. They capture velocity in both the streamwise and cross-stream directions on planview geometries in the horizontal. 3D models are similar to 2D, but solve an even more complex full system of equations using finite difference (e.g. ROMS – Warner et al., 2008), finite volume (e.g. Fast3d – Landsberg et al., 1998) or finite element based methods. They are thus potentially more accurate, but considerably more computationally expensive. Established modelling frameworks offer 2D and 3D options, such as Telemac-Mascaret (Hervouet, 1999) and Delft3d (Deltares, 2014), which use finite element/volume and finite difference based methods, respectively. In choosing a model, one must balance the simplicity and computational efficiency of a 2D model against the potential accuracy of a 3D one.

Despite this variety of approaches, Syvitski et al. (2010) argue the need for more accurate and faster morphodynamic models. The aim of this work is to present a novel and flexible 2D depth-averaged coupled hydrodynamic and sediment transport model developed within *Thetis*, a finite element coastal ocean modelling system (Kärnä et al., 2018) built using the *Firedrake* code generation framework (Rathgeber et al., 2017). This framework is versatile and ensures the underlying code is robust and optimised, and can be executed efficiently in parallel. Furthermore, it means our model is easily extensible and further work could include using an adjoint allowing sensitivity analyses to be

Author credits

Mariana C. A. Clare: Code development and verification, experimental design, manuscript preparation. **James R. Percival:** Technical supervision, manuscript review and editing. **Athanasios Angeloudis:** Technical supervision, manuscript review and editing. **Colin J. Cotter:** Project supervision, manuscript review and editing. **Matthew D. Piggott:** Project supervision, manuscript review and editing.

Email addresses

 m.clare17@imperial.ac.uk (M.C.A. Clare)

32 conducted (Farrell et al., 2013) or using an adaptive mesh to further decrease computational cost (McManus et al.,
33 2017).

34 In this work, a 2D model is deemed appropriate because the depth-scale is much smaller than the horizontal for
35 the cases discussed. We extend *Thetis*' existing capability to model scalar transport to simulate suspended sediment
36 transport and introduce a new capability to model bedload transport. For validation purposes, our results are compared
37 with experimental data and the widely used Telemac-Mascaret's 2D model (Hervouet, 1999) (Amoudry and Souza,
38 2011; Papanicolaou et al., 2008). We improve on existing state-of-the-art models by using a discontinuous Galerkin
39 based finite element discretisation (DG) available in *Thetis* (Kärnä et al., 2018). DG has several advantages including
40 being locally mass conservative, meaning sediment is conserved on an element-by-element level, which is an advantage
41 for coupling (Dawson, Sun and Wheeler, 2004); being well-suited to advection-dominated problems (Kärnä et al.,
42 2018); being geometrically flexible; and allowing higher order local approximations (Li, 2006). Morphodynamic
43 models using DG have been presented in Kubatko, Westerink and Dawson (2006), Michoski et al. (2013) and Tassi et al.
44 (2008), but without suspended sediment transport. To the best of our knowledge, our model is the first morphodynamic
45 model with both bedload and suspended sediment transport to use DG.

46 The remainder of this paper is structured as follows: in Section 2 we describe our coupled hydrodynamic and
47 sediment transport model; in Section 3 we outline details of the finite element model *Thetis*; in Sections 4 and 5, we
48 employ the test cases of a migrating trench and a meander to validate our model and in Section 6 we benchmark our
49 test cases against Telemac-Mascaret's 2D model.

50 2. Model derivation

51 2.1. Hydrodynamic and sediment transport equations

52 In this subsection, we describe the general equations for modelling the hydrodynamic and sediment transport flow,
53 and follow the presentation and notation of Wu (2007), where more details can be found. The hydrodynamic component
54 of the sediment-water mixture is governed by the (3D) Navier-Stokes equations for single phase flow. We use the 2D
55 version of *Thetis* assuming the only external force acting on the system is gravity. We also assume any wavelength
56 is much longer than the depth of the fluid, hence the vertical flow variation is small enough to be negligible and
57 $\partial u_1 / \partial z = \partial u_2 / \partial z = 0$ (for more details, see Segur, 2009).

The 2D model is derived by depth-averaging from the bed, z_b , to the water surface, η , the hydrodynamic equations.
Thus, we apply the kinematic boundary condition at η as a free moving boundary, and we consider z_b to be imper-
meable. Since the bed evolution is slow, imposing a no-slip condition at z_b means $u_1 = u_2 = 0$ here and the simplified
depth-averaged equation for the conservation of mass is

$$\frac{\partial \eta}{\partial t} + \frac{\partial}{\partial x}(h\bar{u}_1) + \frac{\partial}{\partial y}(h\bar{u}_2) = 0, \quad (1)$$

58 where $h = \eta - z_b$ is the depth, and \bar{u}_1 and \bar{u}_2 are the depth-averaged velocities in the x and y directions, respectively.
59 Note that following convention, depth-averaged variables are denoted with an overbar, as $\bar{\cdot}$.

Applying the boundary conditions, combining dispersion and stress effects, and assuming no wind-driving forces
on the water surface, the depth-averaged equation for the conservation of momentum is

$$\frac{\partial(h\bar{u}_i)}{\partial t} + \frac{\partial(h\bar{u}_1\bar{u}_i)}{\partial x} + \frac{\partial(h\bar{u}_2\bar{u}_i)}{\partial y} = -gh\frac{\partial \eta}{\partial x_i} + \frac{1}{\rho}\frac{\partial(h\bar{\tau}_{i1})}{\partial x} + \frac{1}{\rho}\frac{\partial(h\bar{\tau}_{i2})}{\partial y} - \frac{\tau_{bi}}{\rho}, \quad (2)$$

60 where, following the notation of Wu (2007), $\bar{\tau}_{ij} = \mu_t \left(\frac{\partial \bar{u}_i}{\partial x_j} + \frac{\partial \bar{u}_j}{\partial x_i} \right)$ and μ_t is the dynamic eddy viscosity. Note that
61 $i = 1, 2$ represents the x, y -direction respectively. Eq. (1) and (2) comprise the hydrodynamic component of our model.

62 We take an Eulerian approach for the sediment transport equations, rather than the more computationally expen-
63 sive Lagrangian approach, and make a macroscopic assumption. The sediment dynamics are thus represented via an
64 advection-diffusion equation for a sediment concentration field, c . Note that in this work only non-cohesive sediment
65 is considered.

If the sediment diameter is finer than 1 mm and the sediment concentration, c , is lower than 10% of the fluid volume
then we can assume there is no mixing at the 'molecular level'. Hence, there is no diffusion and the only significant
relative motion between the flow and the sediment is settling due to gravity. The low concentration and fine sediment

size means the settling velocity of the sediment particles w_s can be approximated by that of a single sediment particle in clear water. The equation governing the sediment concentration is

$$\frac{\partial c}{\partial t} + \frac{\partial(u_1 c)}{\partial x} + \frac{\partial(u_2 c)}{\partial y} + \frac{\partial(u_3 c)}{\partial z} = \frac{\partial}{\partial x}(w_s c \delta_{31}) + \frac{\partial}{\partial y}(w_s c \delta_{32}) + \frac{\partial}{\partial z}(w_s c \delta_{33}), \quad (3)$$

where δ_{3j} is the Kronecker delta applied to the vertical component. Time-averaging Eq. (3) to filter turbulence introduces a diffusivity term, $\epsilon_s \nabla \cdot c$, and reads

$$\frac{\partial c}{\partial t} + \frac{\partial(u_1 c)}{\partial x} + \frac{\partial(u_2 c)}{\partial y} + \frac{\partial(u_3 c)}{\partial z} - \frac{\partial(w_s c)}{\partial z} = \frac{\partial}{\partial x} \left(\epsilon_s \frac{\partial c}{\partial x} \right) + \frac{\partial}{\partial y} \left(\epsilon_s \frac{\partial c}{\partial y} \right) + \frac{\partial}{\partial z} \left(\epsilon_s \frac{\partial c}{\partial z} \right), \quad (4)$$

66 where ϵ_s is the so-called sediment turbulent diffusivity coefficient, which can be chosen to take a larger than physically
67 realistic value as an approximation for unresolved turbulence effects.

As bedload transport occurs along the bed and suspended sediment transport occurs through the fluid water column, the domain is conceptually divided into bedload and suspended sediment zones with an interface at $z = z_b + \delta$ consistent with Tassi and Villaret (2014). At this interface, we define a gradient boundary condition of $E_b = -\epsilon_s \frac{\partial c}{\partial z} |_{z=z_b+\delta} = w_s c_{b*}$ and $D_b = w_s c_b$, where E_b is the near-bed sediment erosion flux, D_b the deposition flux. As δ is assumed to be small, following standard practice, the boundary condition is applied at $z = z_b$. Therefore, depth-averaging Eq. (4), combining the diffusion and dispersion effects, and recalling we are modelling a long-term sedimentation process, we obtain the following non-conservative equation

$$\frac{\partial \bar{c}}{\partial t} + \frac{\partial}{\partial x} (\bar{u}_1 \bar{c}) + \frac{\partial}{\partial y} (\bar{u}_2 \bar{c}) = \frac{\partial}{\partial x} \left(\epsilon_s \frac{\partial \bar{c}}{\partial x} \right) + \frac{\partial}{\partial y} \left(\epsilon_s \frac{\partial \bar{c}}{\partial y} \right) + \frac{E_b - D_b}{h}, \quad (5)$$

68 where we have chosen to implement a non conservative form for the diffusion term, since the discrepancy is small.

Due to the coupled nature of our model, we cannot calculate $\bar{\mathbf{u}}\bar{c}$, but only the product of $\bar{\mathbf{u}}$ (from the hydrodynamic component) and \bar{c} (from the sediment transport component). These two quantities are not equal because the product of two integrated variables is not equal to the integral of their product. Thus, following Huybrechts, Villaret and Hervouet (2010), we rewrite Eq. (5) as an advection-diffusion equation for \bar{c}

$$\frac{\partial \bar{c}}{\partial t} + \frac{\partial}{\partial x} (u_{adv1} \bar{c}) + \frac{\partial}{\partial y} (u_{adv2} \bar{c}) = \frac{\partial}{\partial x} \left(\epsilon_s \frac{\partial \bar{c}}{\partial x} \right) + \frac{\partial}{\partial y} \left(\epsilon_s \frac{\partial \bar{c}}{\partial y} \right) + \frac{E_b - D_b}{h}, \quad (6)$$

with advection velocity

$$\mathbf{u}_{adv} = \frac{\bar{\mathbf{u}}\bar{c}}{\bar{c}}. \quad (7)$$

We then use a correction factor $F_{corr} = \mathbf{u}_{adv}/\bar{\mathbf{u}}$ to convert $\bar{\mathbf{u}}$ into \mathbf{u}_{adv} . Continuing to follow Huybrechts, Villaret and Hervouet (2010), if we assume \mathbf{u} has a logarithmic profile and c has a Rouse concentration profile, we obtain

$$F_{corr} = \frac{I_2 - \log\left(\frac{B}{30}\right) I_1}{I_1 \log\left(\frac{eB}{30}\right)}, \quad (8)$$

where

$$I_1 = \int_{B^{-1}}^1 \left(\frac{(1-a)}{a} \right)^R da, \quad (9a)$$

$$I_2 = \int_{B^{-1}}^1 \log a \left(\frac{(1-a)}{a} \right)^R da, \quad (9b)$$

with $a = z/h$, $B = h/k'_s$, where $k'_s = 3d_{50}$ is the grain roughness coefficient, and $R = w_s/\kappa u_*$ the Rouse number, where κ the Von Kármán constant (given as 0.4 in Wu, 2007) and u_* the shear velocity. To avoid numerical integration, the Rouse concentration profile is simplified, such that Eq. (9) becomes

$$I_1 = \begin{cases} \frac{1}{1-R} (1 - B^{1-R}), & R \neq 1, \\ -\log(B), & R = 1, \end{cases} \quad (10a)$$

$$I_2 = \begin{cases} \frac{I_1 + \log(B)B^{1-R}}{R-1}, & R \neq 1, \\ -0.5(\log(B))^2, & R = 1. \end{cases} \quad (10b)$$

Finally, the sediment concentration equation is

$$\frac{\partial \bar{c}}{\partial t} + \frac{\partial}{\partial x}(F_{\text{corr}} \bar{u}_1 \bar{c}) + \frac{\partial}{\partial y}(F_{\text{corr}} \bar{u}_2 \bar{c}) = \frac{\partial}{\partial x} \left(\epsilon_s \frac{\partial \bar{c}}{\partial x} \right) + \frac{\partial}{\partial y} \left(\epsilon_s \frac{\partial \bar{c}}{\partial y} \right) + \frac{E_b - D_b}{h}. \quad (11)$$

69 2.2. Suspended Sediment Transport

To fully describe Eq. (11), we calculate the sediment source term, $E_b - D_b$, where E_b is the erosion flux and D_b the deposition flux. From the gradient boundary condition, we recall that

$$E_b - D_b = w_s c_{b*} - w_s c_b = w_s c_{b*} - w_s \alpha_c \bar{c}, \quad (12)$$

where w_s is the settling velocity of the particles, c_{b*} the equilibrium near-bed sediment concentration, $c_b = \alpha_c \bar{c}$ the actual near-bed sediment concentration, and α_c a coefficient greater than 1 which accounts for the near-bed sediment concentration value being higher than \bar{c} due to gravity. We choose to approximate α_c using the following formula derived in Tassi and Villaret (2014),

$$\frac{1}{\alpha_c} = \begin{cases} \left| \frac{A(1-A^r)}{r} \right|, & |R-1| > 10^{-4}, \\ |-A \log(A)|, & |R-1| \leq 10^{-4}, \end{cases} \quad (13)$$

where

$$r = \begin{cases} \min(R-1, 3), & |R-1| > 10^{-4}, \\ 0, & |R-1| \leq 10^{-4}, \end{cases} \quad (14)$$

$A = \max\left(\frac{\delta}{h}, 1\right)$, R the Rouse number, and δ the height of the bedload zone. We calculate w_s in Eq. (12) as per Van Rijn (1984), so that

$$w_s = \begin{cases} \frac{g \Delta d_{50}^2}{18\nu}, & d_{50} \leq 10^{-4}, \\ \frac{10\nu}{d_{50}} \left(\sqrt{1 + 0.01 \frac{g \Delta d_{50}^3}{\nu^2}} - 1 \right), & 10^{-4} \leq d_{50} \leq 10^{-3}, \\ 1.1 \sqrt{g \Delta d_{50}}, & d_{50} > 10^{-3}, \end{cases} \quad (15)$$

where d_{50} is the median sediment diameter, ν the kinematic molecular viscosity, and

$$\Delta = \frac{\rho_s}{\rho_f} - 1, \quad (16)$$

70 where ρ_s is the sediment density, and ρ_f the water density.

As discussed in Garcia and Parker (1991), there are alternative formulae for c_{b*} in Eq. (12). In this work, the following formula is used, which is applicable for fine sediments when no waves are present, and is given by Van Rijn (1984) as

$$c_{b*} = 0.015 \frac{d_{50}}{\delta} \frac{S_0^{3/2}}{d_*^{3/10}}, \quad (17)$$

where d_* is the non-dimensional diameter

$$d_* = d_{50} \left(\frac{g \Delta}{\nu^2} \right)^{1/3}, \quad (18)$$

and S_0 the transport stage parameter

$$S_0 = \frac{\Psi \tau_b - \tau_c}{\tau_c}. \quad (19)$$

See Tassi and Villaret (2014) for more detail. In Eq. (19), τ_c is the critical shear stress

$$\tau_c = (\rho_s - \rho_f) g d_{50} \theta_{cr}, \quad (20)$$

where θ_{cr} is the critical Shields parameter; τ_b is the bed shear stress acting against the velocity flow and equal in magnitude in both directions

$$\tau_b = \frac{1}{2} \rho_f C_h (\bar{u}_1^2 + \bar{u}_2^2), \quad (21)$$

where (\bar{u}_1, \bar{u}_2) is the depth-averaged velocity; and Ψ is the skin friction correction

$$\Psi = \frac{C'_h}{C_h} \quad (22)$$

where C_h is the Nikuradse quadratic drag coefficient

$$C_h = 2 \frac{\kappa^2}{\log\left(\frac{11.036h}{k_s}\right)^2}, \quad (23)$$

71 where k_s is the Nikuradse friction height and C'_h is the Nikuradse quadratic drag coefficient using k'_s (the grain rough-
72 ness coefficient defined after Eq. (9)) instead of k_s . C'_h represents the actual skin friction in our model.

73 2.3. Bedload transport

Following Tassi and Villaret (2014), to model bedload transport we define the bedload transport flux, \mathbf{Q}_b

$$\mathbf{Q}_b = \phi_s \sqrt{g \left(\frac{\rho_s}{\rho_f} - 1 \right)} d_{50}^3 (\cos \xi, \sin \xi), \quad (24)$$

where $\cos \xi = \frac{\bar{u}_1}{\sqrt{\bar{u}_1^2 + \bar{u}_2^2}}$ and $\sin \xi = \frac{\bar{u}_2}{\sqrt{\bar{u}_1^2 + \bar{u}_2^2}}$. We choose the Meyer-Peter-Müller formula to define the non-dimensional sediment rate ϕ_s

$$\phi_s = \begin{cases} 0, & \theta' < \theta_{cr}, \\ \alpha_{MPM} (\theta' - \theta_{cr})^{3/2}, & \text{otherwise,} \end{cases} \quad (25)$$

where θ_{cr} is the critical Shields parameter, α_{MPM} a coefficient equal to 8, as suggested by Tassi and Villaret (2014), and θ' the non-dimensional Shields parameter

$$\theta' = \frac{\Psi \tau_b}{(\rho_s - \rho_f) g d_{50}}, \quad (26)$$

74 with Ψ given by Eq. (19) and τ_b by Eq. (21).

75 2.3.1. Slope effect

76 In practice, the magnitude and direction of \mathbf{Q}_b depends on the gradient of the bed, but this is not reflected in Eq.
77 (24). When the bed has a positive gradient in the transport direction, gravity acts against the sediment causing the
78 magnitude of \mathbf{Q}_b to decrease and its direction to alter, and vice versa for a negative gradient.

79 (i) *Magnitude correction*

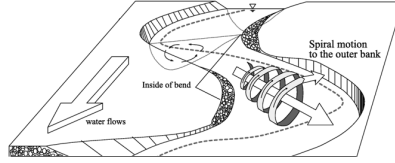


Figure 1: Secondary current in curved channel, adapted from Park and Ahn (2019).

In correcting the magnitude we use

$$\mathbf{Q}_{b*} = \mathbf{Q}_b \left(1 - \Upsilon \frac{\partial z_b}{\partial s} \right), \quad (27)$$

80 given in Soulsby (1997), where s is a direction tangential to the current and Υ an empirical coefficient set to 1.3 (Tassi
81 and Villaret, 2014).

82 (ii) *Angle correction*

Following Talmon, Struiksmas and Mierlo (1995), we set

$$T = \frac{1}{\beta_2 \sqrt{\theta}}, \quad (28)$$

where β_2 is an empirical coefficient (equal to 1.5 for river test cases) and θ is given by

$$\theta = \frac{(\rho_f - \rho_s) g d_{50}}{\max\left(\frac{1}{2} \rho_f C_h \|\bar{\mathbf{u}}\|^2, 10^{-10}\right)}, \quad (29)$$

with C_h defined as in Eq. (23). Thus

$$\mathbf{Q}_b = \left(\phi_s \sqrt{g \left(\frac{\rho_s}{\rho_f} - 1 \right) d_{50}^3} (\cos \alpha, \sin \alpha) \right), \quad (30)$$

where α is the corrected angle defined by

$$\begin{pmatrix} \sin \alpha \\ \cos \alpha \end{pmatrix} = \frac{1}{\|\mathbf{p}\|^2} \begin{pmatrix} p_1 \\ p_2 \end{pmatrix} = \frac{1}{\|\mathbf{p}\|^2} \begin{pmatrix} \sin \xi - T \left(\frac{\partial z_b}{\partial y} \right) \\ \cos \xi - T \left(\frac{\partial z_b}{\partial x} \right) \end{pmatrix}, \quad (31)$$

83 where $\mathbf{p} = (p_1, p_2)$.

84 2.3.2. Secondary current

As illustrated in Figure 1, depth-averaged models for curved channels need to account for both the current and helical flow effects. This affects the magnitude and direction of \mathbf{Q}_b and in Tassi and Villaret (2014) is implemented on top of slope effect corrections. Accordingly, we implement a secondary current using

$$\tan \zeta = 7 \frac{h}{r}, \quad (32)$$

given in Engelund (1974), where ζ is the angle between the bedload transport and the main flow direction, h the mean water depth, and r the local radius of curvature of the streamline calculated using

$$r = \frac{\alpha' (\bar{u}_1^2 + \bar{u}_2^2)}{g \frac{\partial \eta}{\partial n}}, \quad (33)$$

85 where η is the elevation, n a direction normal to the current and α' a coefficient which lies between 0.75 (rough bed)
86 and 1 (smooth bed).

Using Eq. (32), we construct the term

$$\Xi = \sqrt{(\tau_b \Upsilon \cos \alpha + \tau_b \bar{u}_2 \tan \zeta)^2 + (\tau_b \Upsilon \sin \alpha - \tau_b \bar{u}_1 \tan \zeta)^2}, \quad (34)$$

where τ_b is the bedload shear stress defined by Eq. (21), and α and Υ are the corrected flow angle and magnitude factors (Section 2.3.1).

Hence, we define a new corrected bed transport flow direction $\hat{\alpha}$ with

$$\cos \hat{\alpha} = \frac{\tau_b \Upsilon \cos \alpha + \tau_b \bar{u}_2 \tan \zeta}{\Xi}, \quad (35a)$$

$$\sin \hat{\alpha} = \frac{\tau_b \Upsilon \sin \alpha - \tau_b \bar{u}_1 \tan \zeta}{\Xi}, \quad (35b)$$

and a new slope magnitude correction factor

$$\hat{\Upsilon} = \frac{\Xi}{\tau_b}. \quad (36)$$

Note that if a secondary current effect is imposed without slope effect corrections, then $\Upsilon = 1$ and $\alpha = \xi$, *i.e.* the original flow angle.

2.4. Calculating the new bedlevel

The new bedlevel, z_b , is affected by both the suspended sediment and bedload transport described in Sections 2.2 and 2.3, and is governed by the Exner equation

$$(1 - p') \frac{dz_b}{dt} + \nabla_h \cdot \mathbf{Q}_b = D_b - E_b, \quad (37)$$

where p' is the bed sediment porosity. This completes the model equations.

2.5. Practical application within the *Thetis* framework

When implementing our model, two common techniques for algorithm stability and efficiency reasons are adopted as follows:

2.5.1. Spinning up the hydrodynamics

Once the simulation starts, we are forcing a previously motionless flow, and the resulting flow instabilities could trigger unrealistic bedlevel changes. Following standard practice (e.g. Gerritsen et al., 2008), we avoid this by first running a simulation solving only the hydrodynamic equations. Once the velocity and elevation fields have reached a quasi-steady state, we trigger sediment and bedlevel changes.

2.5.2. Morphological scale factor

Once running a bed evolution simulation for a long period of time, a morphological scale factor, m , is often used (e.g. Gerritsen et al., 2008) which amplifies the rate of bedlevel changes to save computational time. This factor means that each Δt in the hydrodynamic and sediment concentration equations is equivalent to $m\Delta t$ for the bed evolution. We implement this by including the factor m in the Exner equation (37)

$$\frac{(1 - p')}{m} \frac{dz_b}{dt} + \nabla_h \cdot \mathbf{Q}_b = D_b - E_b. \quad (38)$$

This factor is suitable because the hydrodynamics are in an approximate steady state, and we assume throughout that changes in the bed are significantly slower than in the hydrodynamics.

3. Finite element based implementation

We build on existing elements of *Thetis* for the implementation of a coupled hydrodynamic and sediment transport model. *Thetis* is a finite element coastal ocean modelling system (built using the code generating framework *Fire Drake*)

107 which is first described in Kärnä et al. (2018) with a 3D model. We use the 2D depth-averaged version of *Thetis* outlined
 108 in Vouriot et al. (2019), which solves the shallow water equations and the non-conservative form of a depth-averaged
 109 sediment concentration equation, as discussed in the previous section.

110 We use a discontinuous Galerkin based finite element discretisation (DG) which has several advantages in this
 111 context, as discussed in Section 1.

112 3.1. DG based methods in *Thetis*

When using DG based methods, we generate an unstructured mesh of triangular elements tessellating our domain Ω and define our finite element space on this mesh. Using a discontinuous function space requires the definition of variables on element edges (including on the domain boundary $d\Omega$), with the union of these edges denoted by Γ . The average operator $\{\{\cdot\}\}$ and jump operator $[[\cdot]]$ across the interior edges on scalar and vector fields are

$$\begin{aligned} \{\{\mathbf{X}\}\} &= \frac{1}{2}(\mathbf{X}^+ + \mathbf{X}^-), & [[\chi]]_{\mathbf{n}} &= \chi^+ \mathbf{n}^+ + \chi^- \mathbf{n}^-, \\ [[\mathbf{X}]]_{\mathbf{n}} &= \mathbf{X}^+ \cdot \mathbf{n}^+ + \mathbf{X}^- \cdot \mathbf{n}^-, \end{aligned}$$

113 where $\mathbf{n} = (n_x, n_y, 0)$ is the horizontal projection of the outward pointing unit normal on the element edge, and ‘+’ and
 114 ‘-’ denote either side of the interior edge.

115 3.1.1. Depth-averaged sediment concentration equation

116 *Thetis* uses very similar techniques to solve the hydrodynamic equations, (1) and (2), and the sediment concentration
 117 equation (11). We focus on the latter because it is the most pertinent for this work; the formulation for the hydrodynamic
 118 equations can be found in Kärnä et al. (2018), Pan, Kramer and Piggott (2019) and Vouriot et al. (2019).

To define the sediment concentration on the element edges, *Thetis* uses an upwinding scheme, \bar{c} : at each edge, \bar{c} is chosen to be equal to its upstream value with respect to velocity, \bar{c}^{up} (see Leveque, 1996). We discretise the sediment concentration equation (11) using the implicit Backward Euler timestepping method. The starting point for our numerical implementation is the following weak form

$$\int_{\Omega} \psi \left(\frac{\bar{c}_i^{(n+1)} - \bar{c}_i^{(n)}}{\Delta t} \right) dx + \int_{\Omega} \psi \mathbf{u}_i^{(n+1)} \cdot \nabla_h \bar{c}_i^{(n+1)} dx - \int_{\Omega} \psi \nabla_h \cdot \left(\epsilon_s \nabla_h \bar{c}_i^{(n+1)} \right) dx = \int_{\Omega} \psi \left(E_{b_i}^n - D_{b_i}^n \right) dx, \quad (39)$$

119 where ψ is the test function employed in the weak formulation of the finite element method. Note that as E_b and D_b
 120 are calculated explicitly using (12), the full formulation is semi-implicit.

Several choices can be made to reach the final form used in the model. We choose to integrate the advection term by parts to obtain a boundary integral term, which allows the imposition of boundary conditions on our equation and the fluxes between elements on the element boundaries to be controlled. Thus the weak form of the advection term becomes

$$\int_{\Omega} \psi \bar{\mathbf{u}} \cdot \nabla_h \bar{c} dx = - \int_{\Omega} \bar{c} \nabla_h \cdot (\bar{\mathbf{u}} \psi) dx + \int_{\Gamma} \bar{c}^{\text{up}} [[\psi \bar{\mathbf{u}}]]_{\mathbf{n}} ds. \quad (40)$$

For the diffusivity term, we must transform the second order derivative to a first order one since the equations are solved using a piecewise linear function space. Following Kärnä et al. (2018), we thus integrate by parts, applying the Symmetric Interior Penalty Galerkin (SIPG) method given in Epshteyn and Rivière (2007) to ensure the discretisation is stable. Thus the weak form of the diffusivity term becomes

$$\begin{aligned} - \int_{\Omega} \psi \nabla_h \cdot (\epsilon_s \nabla_h \bar{c}) dx &= \int_{\Omega} \epsilon_s (\nabla_h \psi) \cdot (\nabla_h \bar{c}) dx - \int_{\Gamma} [[\psi]]_{\mathbf{n}} \cdot \{\{\epsilon_s \nabla_h \bar{c}\}\} ds - \int_{\Gamma} [[\bar{c}]]_{\mathbf{n}} \cdot \{\{\epsilon_s \nabla_h \psi\}\} ds \\ &\quad + \int_{\Gamma} \sigma \{\{\epsilon_s\}\} [[\bar{c}]]_{\mathbf{n}} \cdot [[\psi]]_{\mathbf{n}} ds. \end{aligned} \quad (41)$$

121 where σ is the penalty parameter of the SIPG method given in Kärnä et al. (2018).

122 To solve the full sediment concentration weak form equation, *Thetis* formulates the equation as a matrix problem
 123 for $c^{(n+1)}$ and uses the generalised minimal residual method (GMRES) to solve the system (see Jacobs and Piggott

124 (2015)). The use of upwinded numerical fluxes and slope limiters means our model is robust at modelling steep bed
 125 gradients formed such as those in the migrating trench test case in Section 4 (see Kubatko, Westerink and Dawson,
 126 2006). Furthermore, the combination of a DG based method with a semi-implicit timestepping method makes our
 127 model very stable.

128 3.1.2. Exner Equation

In order to avoid grid-scale noise and unstable oscillations in solving the Exner equation (37), we define the bedlevel, z_b , on a continuous grid, and thus use a continuous Galerkin based finite element discretisation (CG). We project all hydrodynamic and sediment transport variables from the DG space into the CG space before calculating the terms in the Exner equation. This causes a minor loss of accuracy in model variables, but overall a more stable bedlevel result. The weak form of the divergence term $\nabla_h \cdot \mathbf{Q}_b$ is

$$\int_{\Omega} \psi \nabla_h \cdot \mathbf{Q}_b dx = - \int_{d\Omega} (\mathbf{Q}_b \cdot \mathbf{n}) \psi ds + \int_{\Omega} (\mathbf{Q}_b \cdot \nabla_h) \psi dx. \quad (42)$$

Here the only boundary contribution is from the domain boundary $d\Omega$ because we are on a continuous grid and are assuming centred fluxes on interior edges. Therefore the values on either side of each interior edge cancel over the whole domain. We use the implicit backward Euler method to solve Eq. (37) allowing us to use large timesteps stably. Thus

$$\int_{\Omega} \left((1 - p') \frac{z_{b_i}^{(n+1)} - z_{b_i}^{(n)}}{\Delta t} \right) \psi dx = G_i^{(n+1)}, \quad (43)$$

129 where $G_i^{(n+1)}$ is the sum of the weak form of the source term (as in (39)) and (42). Note that the radius of curvature,
 130 (33), in the secondary current parametrisation is dependent on the surface elevation η rather than on z_b . Hence, we
 131 rewrite η as $(h + z_b)$ meaning we can benefit from an implicit discretisation.

132 4. Migrating trench test case

133 We consider the simple test case of a migrating trench (as in, for example, Gerritsen et al. 2008 and Van Rijn 1980)
 134 to validate the implementation of the mathematical and numerical methods used in *Thetis*, by using experimental data
 135 from a lab study in Van Rijn (1980) and results from Villaret et al. (2016).

136 In Villaret et al. (2016), for this test case, a coupled model is used comprising Telemac-Mascaret's 2D depth-
 137 averaged hydrodynamic module, Telemac2D, and its sediment transport and bed evolution module, *Sisyphé*. We refer
 138 to this coupled model as *Sisyphé*. For the discretisation, they use Telemac-Mascaret's continuous finite element model
 139 (Danilov, 2013) with the method of characteristics for the hydrodynamic advection terms and distributive schemes
 140 for the sediment transport advection terms. The method of characteristics has the advantage of being unconditionally
 141 stable, but is not mass conservative and is diffusive for small timesteps, meaning the problem is artificially regularised
 142 with potentially spurious mixing. Distributive schemes are mass conservative, but also have high numerical diffusion
 143 and Courant number limitations to ensure stability. For further details on both methods, see Hervouet (2007) and Tassi
 144 and Villaret (2014). The limitations of these two methods in part motivate our use of DG based methods in *Thetis*.

145 4.1. Test case configuration

146 In Figure 2, the initial trench profile and the final bedlevel profile after a 15 h experiment is observed demonstrating
 147 the trench migration over time.

148 For *Sisyphé*, we use the model of Villaret et al. (2016), and summarise the parameter values in Table 1. As these
 149 have been calibrated and validated by experiments, *Sisyphé*'s results can assist the validation of our model. Thus, we
 150 use the same parameter values in *Thetis* on a grid of mesh size $\Delta x = 0.2$ m in the x -direction. A coarser $\Delta y = 0.22$ m
 151 is set in the y -direction in our *Thetis* model than Villaret et al. (2016), who applied $\Delta y = 0.11$ m. We found that unlike
 152 in *Sisyphé*, our model results are consistent with either Δy , indicating that our model is more robust. Thus we adopt the
 153 less computationally expensive option. Finally, we use the boundary conditions from Section 2 and set the incoming
 154 suspended sediment flow rate so that the erosion flux, E_b , equals the deposition flux, D_b , at the upstream boundary.
 155 Hence, sediment equilibrium is established at the inlet and the bed remains unaltered.

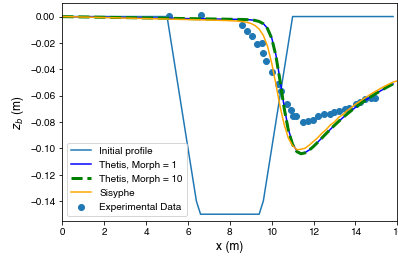


Figure 2: Bedlevel after 15 h for different morphological scale factors comparing experimental data, *Sisyphé* and *Thetis*. Experimental data and initial trench profile source: Villaret et al. (2016).

Table 1

Parameter values for the migrating trench test case Villaret et al. (2016)

Variable Name	Variable Value
Length in x -direction	16 m
Length in y -direction	1.1 m
Morphological simulation time	15 h
Depth	0.397 m
Downstream elevation	0.4 m
Upstream flux	$0.22 \text{ m}^3 \text{ s}^{-1}$
Median particle size (d_{50})	$1.6 \times 10^{-4} \text{ m}$
Sediment density (ρ_s)	2650 kg m^{-3}
Water density (ρ_f)	1000 kg m^{-3}
Kinematic viscosity (ν)	$1 \times 10^{-6} \text{ m}^2 \text{ s}^{-1}$
Bed sediment porosity (p')	0.4
Diffusivity (ϵ_s)	$0.01 \text{ m}^2 \text{ s}^{-1}$
Nikuradse friction height (k_s)	0.025 m

4.2. Results

We run both *Thetis* and *Sisyphé* for this test case. As discussed in Section 2.5, a pure hydrodynamics simulation is run for 200 s ramping up the initial hydrodynamic conditions for our coupled simulation with bedload and suspended sediment transport. We do not use either the slope effect angle correction or secondary current here because both are superfluous in a straight channel.

Figure 2 shows that the bedlevel results from *Thetis* and *Sisyphé* agree in both magnitude and profile, but are clearly different from the experimental data. By contrast, when Villaret et al. (2016) use the parameter values in Table 1, the *Sisyphé* results agree with the experimental data. The difference between the two set-ups is the timestep, Δt : Villaret et al. (2016) use $\Delta t = 1 \text{ s}$, whereas we use $\Delta t = 0.05 \text{ s}$ in Figure 2. This choice of Δt is because *Thetis* requires a smaller Courant number ($U\Delta t/\Delta x$) than *Sisyphé* and for comparability reasons the same Δt is used in both models. A possible explanation of this Courant number requirement in *Thetis* is that the overall model can be perceived as semi-implicit since all model equations are solved implicitly (or semi-implicitly for the sediment concentration equation), while the coupling of the hydrodynamic and sediment transport components is explicit.

Figure 2 also illustrates that using either a morphological scale factor of 10 or 1 in our *Thetis* model gives very similar results. Unless otherwise stated, all figures in this section are produced using a morphological scale factor of 10. Although *Sisyphé* has an option for a morphological scale factor, it is not imposed in this work in *Sisyphé* because neither Villaret et al. (2016) or Villaret et al. (2013) apply it.

4.2.1. Sensitivity study

The dependence of *Sisyphé*'s results on Δt presents a necessity for a sensitivity study on the robustness of the models to small changes in physical parameters, timestep and/or mesh step size. First, we explore the impact of varying Δt and the mesh size Δx on the final bedlevel. Note that once the mesh size Δy is small enough that the results are smooth in *Sisyphé*, it has no effect because there is negligible bedlevel variation in that direction. Figure 3a shows that the *Sisyphé* bedlevel results vary significantly with Δt . Only when $\Delta t = 1 \text{ s}$, the value of Villaret et al. (2016), is there a good agreement between *Sisyphé* and the experimental data. As Δt decreases, *Sisyphé*'s results converge to the same result as *Thetis* in Figure 2. By contrast, bedlevel results from *Thetis* are largely insensitive to changes in Δt , as seen in Figure 3b.

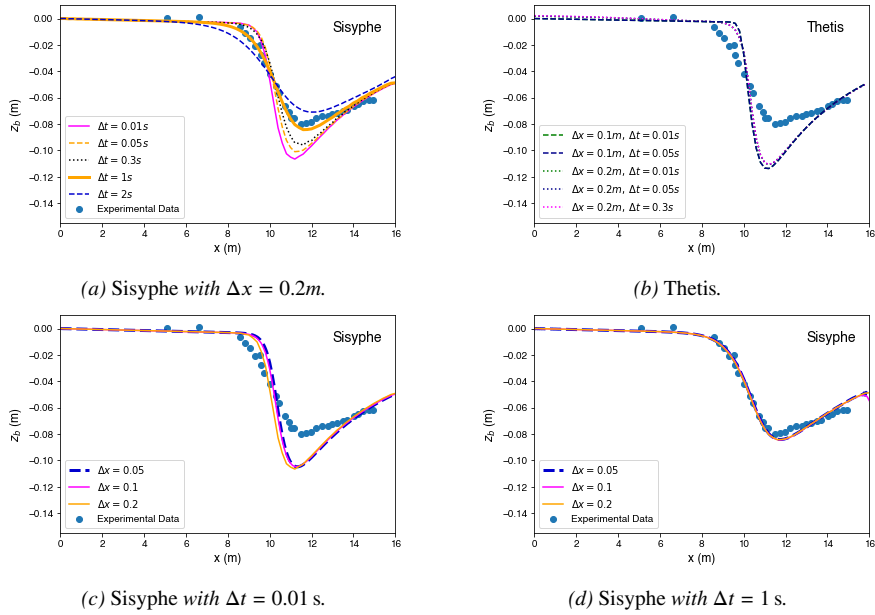


Figure 3: Sensitivity of bedlevel to Δx and Δt .

182 Furthermore, we run a small study to investigate whether *Sisyphes* is always sensitive to Δt for this test case. When
 183 the method of characteristics is chosen for the hydrodynamics, as in Villaret et al. (2016), we find *Sisyphes* is always
 184 sensitive to Δt , independent of the choice of morphodynamic scheme. Other methods for the hydrodynamics have
 185 stricter Courant number criteria, requiring $\Delta t < 0.01$ s to run (even smaller than our *Thetis* value), meaning this effect
 186 is less noticeable.

187 We also run a sensitivity study for Δx and find that for finer meshes than that used in Villaret et al. (2016), both
 188 models were insensitive to Δx (see Figures 3b, 3c and 3d). However, one of the advantages of the DG method is that
 189 it is good at dealing with sharp gradients. To illustrate this we run the test case with a significantly coarser mesh of
 190 $\Delta x = 0.5$ m. Thus in the x -direction, each side of the trench is initially represented by three mesh elements and the flat
 191 bottom of the trench is initially represented by six mesh elements. The mesh nodes are located exactly at the vertices of
 192 the slope, meaning that the initial geometry is accurately represented by this mesh. Figure 4b shows that for our *Thetis*
 193 model there are no observable differences between the coarser and finer meshes. On the other hand, Figure 4a shows
 194 that *Sisyphes* fails to produce an accurate solution. Due to instabilities, the *Sisyphes* solution has also broken symmetry
 195 in the y -direction meaning that it is no longer independent of y , indicating *Sisyphes* has not converged accurately. To
 196 show the solution's dependence on y , in Figure 4a, we show the final bedlevel transects at the beginning ($y = 0.0$ m),
 197 midpoint ($y = 0.55$ m) and end ($y = 1.1$ m) of the domain (recall that in *Sisyphes*, $\Delta y = 0.11$ m). By contrast in Figure
 198 4b, as in the other figures in this section, we only need to show the transect at the midpoint because the solution from
 199 our model is effectively independent of y .

200 Given the robustness of *Thetis* from this point onwards all our model results for the migrating trench test case apply
 201 $\Delta x = 0.5$ m and $\Delta t = 0.6$ s. Given the lack of robustness in *Sisyphes* from this point onwards all our *Sisyphes* model
 202 results for the migrating trench test case use $\Delta t = 0.01$ s.

203 For small values of Δt , *Thetis* and *Sisyphes* are consistent. We conjecture that the errors caused in *Sisyphes* with
 204 larger Δt values manifest themselves as an increase in effective diffusivity in the model. We thus conduct a sensitivity
 205 study for the sediment turbulent diffusivity coefficient, ϵ_s . For this study, we choose $\Delta t = 0.01$ s in *Sisyphes*. Bedlevel
 206 results from both *Sisyphes* and *Thetis* in Figures 5a and 5b show they are indeed greatly affected by ϵ_s and, importantly,
 207 that both models behave consistently. Note that, due to stability constraints, *Sisyphes* does not run with $\epsilon_s > 0.2$ m² s⁻¹,
 208 unlike *Thetis*. The observed sensitivity to ϵ_s is to be expected because the grid Peclet number ($U\Delta x/\epsilon_s$) decreases
 209 with ϵ_s , making diffusion the key driver of the sediment concentration equation, rather than advection. Thus, we can
 210 use ϵ_s to calibrate both models; in *Sisyphes*, Δt can be used to similar effect. If we set $\epsilon_s = 0.15$ m² s⁻¹, *Thetis* and
 211 *Sisyphes*'s converged results agree well with each other and with the experimental data, as shown clearly in Figure 6.
 212 Thus, we have validated *Thetis* for this simple test case.

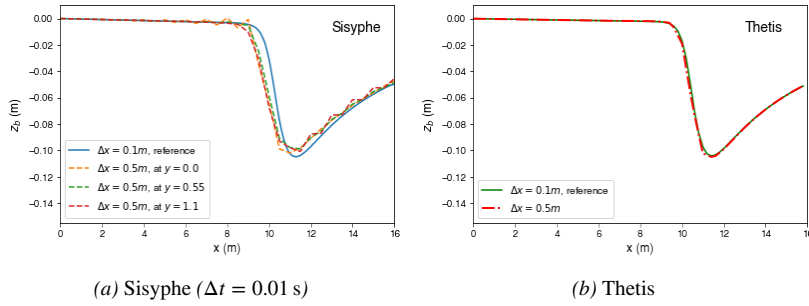


Figure 4: Bedlevel using a very coarse mesh ($\Delta x = 0.5$ m) compared with a fine mesh ($\Delta x = 0.1$ m) for reference.

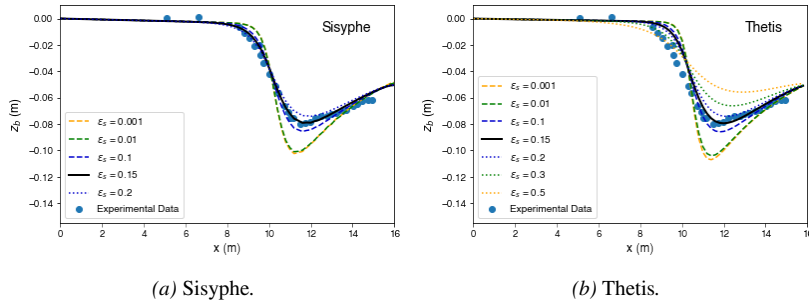


Figure 5: Sensitivity of bedlevel to diffusivity.

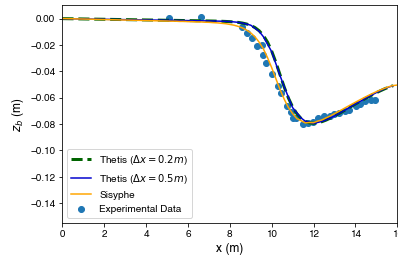


Figure 6: Bedlevel from *Thetis* and *Sisyphé* after 15 h using $\epsilon_s = 0.15\text{m}^2/\text{s}$.

213 5. Meander test case

214 Our second test case regards the curved channel of a meander, which requires and demonstrates the implementa-
 215 tion of a slope effect angle correction and a secondary current. This test case is used to validate these additional
 216 functionalities, and affirm our model can handle more complex and realistic set-ups.

217 5.1. Test case configuration

218 We use the configuration from experiment 4 from Yen and Lee (1995) and validate *Thetis* through the experimental
 219 data and *Sisyphé* results from Villaret et al. (2013). Most of the bed changes occur at the boundary so, following Villaret
 220 et al. (2013), we use a finer mesh there (0.1 m) and a coarser one (0.25 m) along the centre of the channel, as in Figure
 221 7.

222 We impose time dependent flux and elevation boundary conditions reproducing Yen and Lee (1995). The initial
 223 inflow flux and outflow elevation are $0.02\text{ m}^3\text{ s}^{-1}$ and 0 m, respectively. Both increase linearly until reaching their
 224 respective maximums of $0.053\text{ m}^3\text{ s}^{-1}$ and 0.103 m at 100 min, and then decrease linearly to their initial values at 5 h.
 225 We also impose a free-slip condition on the meander boundary walls.

226 In both *Thetis* and *Sisyphé*, we use the parameter values summarised in Table 2. Following Villaret et al. (2013),
 227 we only model bedload transport because this is the principal sediment transport component in rivers. Hence, we do

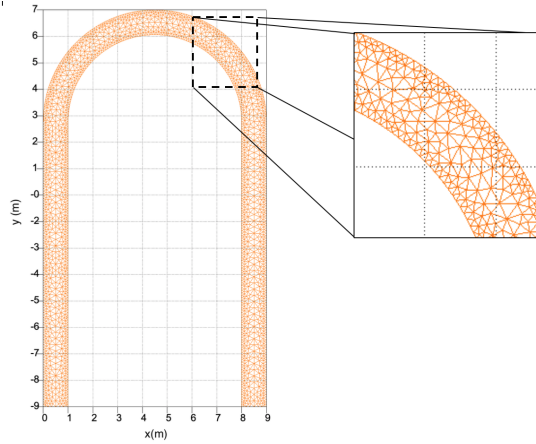


Figure 7: Meander mesh and domain used both in *Thetis* and *Sisyphé* by Villaret et al. (2013).

Table 2

Parameter values for the meander test case Villaret et al. (2013)

Variable Name	Variable Value
Channel width	1 m
Inner radius	3.5 m
Outer radius	4.5 m
Straight reach at channel ends	11.5 m
Morphological simulation time	5 h
Depth	0.0544 m
Median particle size (d_{50})	1×10^{-3} m
Sediment density (ρ_s)	2650 kg m^{-3}
Water density (ρ_f)	1000 kg m^{-3}
Kinematic viscosity (ν)	$0.01 \text{ m}^2 \text{ s}^{-1}$
Bed sediment porosity (p')	0.4
Nikuradse friction height (k_s)	0.0035 m

228 not need to specify the diffusivity coefficient ϵ_s . The implementation of the secondary current requires we determine
 229 the flow roughness to set the value of α' in Eq. (33). Following Kulkarni and Sahoo (2013), we calculate that the
 230 roughness Reynolds number, defined by $(k_s \sqrt{\tau_b}) / (\nu \sqrt{\rho_f})$, is approximately 80, and conclude that the case is subject
 231 to a rough turbulent flow regime. Consistently with Tassi and Villaret (2014), we use $\alpha' = 0.75$.

232 5.2. Results

233 5.2.1. Modelling the hydrodynamics

234 If the same viscosity value is applied when modelling the hydrodynamics for the meander test case as for the
 235 migrating trench test case ($1 \times 10^{-6} \text{ m}^2 \text{ s}^{-1}$), our model does not accurately solve the flow at the meander boundary
 236 walls. Instead of finding a smooth solution, the flow magnitude increases dramatically in cells closest to the boundary.
 237 However molecular viscosity values ($1 \times 10^{-6} \text{ m}^2 \text{ s}^{-1}$) only become relevant at the Kolmogorov scale. This test case
 238 is at a much larger scale where viscous turbulence forces exist. As such the viscosity is accounting for the turbulence
 239 or eddy viscosity and a value of $1 \times 10^{-3} \text{ m}^2 \text{ s}^{-1}$ (the value by Vouriot et al. (2019) for their *Thetis* test case) is more
 240 appropriate. As we increase ν in the hydrodynamic equations (1) and (2) the flow becomes smoother and for viscosity
 241 values of $O(1 \times 10^{-3})$ the boundary issue no longer exists. The issue itself is related to the manner in which boundary
 242 conditions at closed impermeable boundaries are imposed in equal order DG discretisations and will be addressed in
 243 the future.

244 As we are not using a turbulence model, to find the correct value of ν , we use *Sisyphé's* hydrodynamic results to
 245 calibrate our model, noting that Villaret et al. (2013) use $1 \times 10^{-2} \text{ m}^2 \text{ s}^{-1}$. These alterations in ν change the nature of
 246 the test case, but can be balanced by altering the longitudinal bed slope. In Yen and Lee (1995), the meander has a
 247 longitudinal bed slope of 0.002, as in Villaret et al. (2013). We find that for a longitudinal bed slope of 0.0035 and ν
 248 of $0.035 \text{ m}^2 \text{ s}^{-1}$, our model's velocities match those in *Sisyphé* reasonably well, as shown in Figures 8a and 8b. These

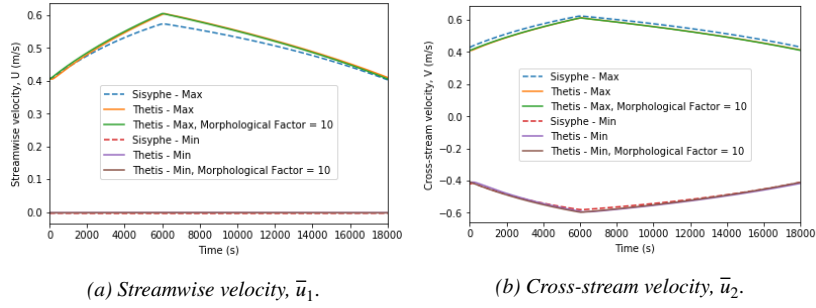


Figure 8: Minimum and maximum velocities from *Thetis* ($\nu = 0.035 \text{ m}^2 \text{ s}^{-1}$, slope = 0.0035) with a morphological scale factor of 1 and 10, and *Sisyphus*, present study, ($\nu = 0.01 \text{ m}^2 \text{ s}^{-1}$, slope = 0.002).

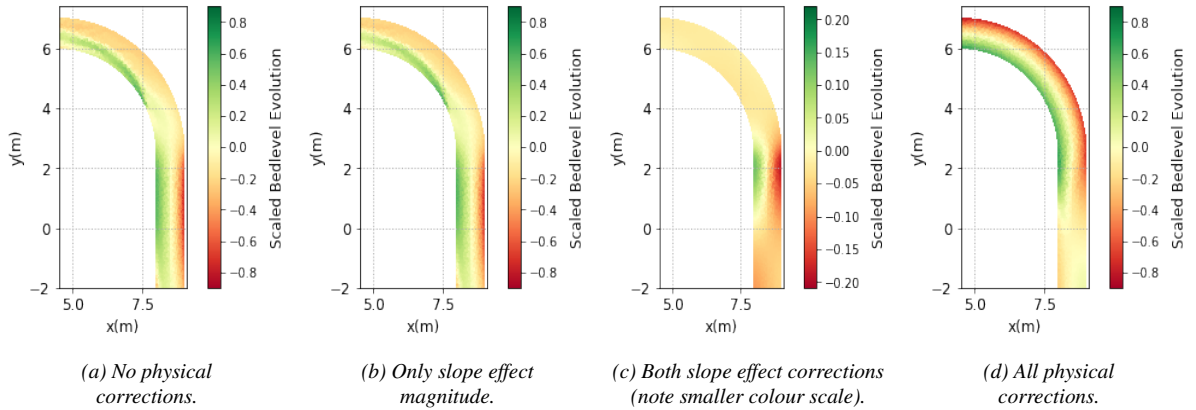


Figure 9: Meander section showing scaled bedlevel evolution from *Thetis* with different physical corrections to Q_b .

249 figures also show that even with time dependent boundary conditions, using a morphological scale factor equal to
 250 either 1 or 10 in *Thetis* gives equivalent results. Thus, unless otherwise stated, in this section our *Thetis* results are
 251 produced with a morphological scale factor of 10.

252 5.2.2. Modelling sediment transport

As the hydrodynamics of *Thetis* agree with *Sisyphus*, we introduce sediment transport into the models. As discussed
 in Section 2.5, initially a simulation for 200 s solves only the hydrodynamics with a fixed flux inflow of $0.02 \text{ m}^3 \text{ s}^{-1}$
 and outflow elevation of 0 m. For our full sediment transport simulation, we use these results as initial flow conditions
 and impose time dependent flux and elevation conditions from Section 5.1 as the boundary conditions. We present the
 scaled bedlevel evolution results, defined as

$$\text{Scaled Bedlevel Evolution} = \frac{z_{\text{final}} - z_{\text{initial}}}{z_{\text{initial}}} \quad (44)$$

253 where z_{final} is the final bedlevel after 5 h and z_{initial} is the initial bedlevel of -0.0544 m .

254 Figure 9 shows the effects of implementing secondary current and slope effects on the bedlevel evolution at the
 255 meander outflow. The slope effect magnitude correction has little effect compared to the secondary current and slope
 256 effect angle corrections, likely because the slopes in this test case are fairly gentle.

257 In Figure 9d, the final scaled bedlevel evolution result is shown, with erosion at the outer bend and deposition at
 258 the inner bed, as expected from physical intuition. Comparing this figure with Figure 10 from Villaret et al. (2013), we
 259 see *Thetis* result has the same distribution and magnitude as the experiment and *Sisyphus*. Hereafter, unless otherwise
 260 stated that the results are from the present study, *Sisyphus* results are taken from those presented in Villaret et al. (2013).

261 To compare our *Thetis* result with the experiment and *Sisyphus*'s results more accurately, we take a cross-section
 262 at the 90° and 180° angles marked on Figure 10. Figures 11a and 11b shows our model reproduces the experimental

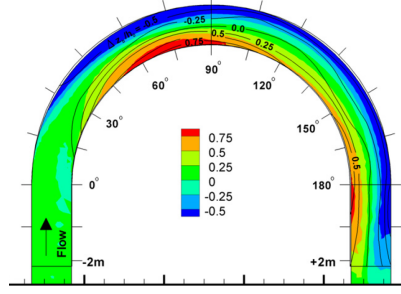


Figure 10: Scaled bedlevel evolution from *Sisyphé* (coloured bars) and experimental data (black contours). Source: Villaret et al. (2013).

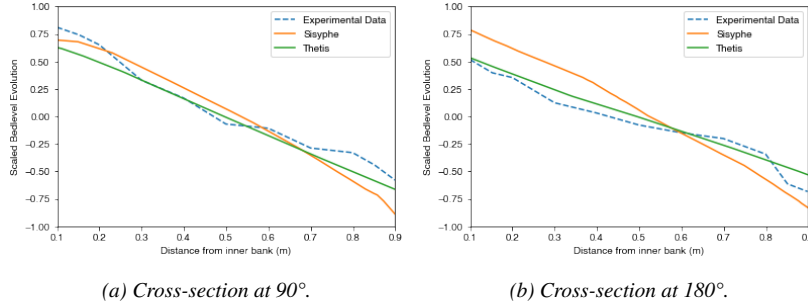


Figure 11: Scaled bedlevel evolution from *Thetis* (with $\nu = 0.035 \text{ m}^2 \text{ s}^{-1}$, slope = 0.0035); *Sisyphé*, Villaret et al. (2013); and experimental data Yen and Lee (1995).

Table 3

Sum of relative error norms for different values of longitudinal slope and $\nu \text{ (m}^2 \text{ s}^{-1}\text{)}$.

Slope	$\nu = 0.025$	$\nu = 0.035$	$\nu = 0.05$	$\nu = 0.075$
0.003	0.5041	0.4934	0.4847	0.4930
0.0035	0.4911	0.4828	0.4752	0.4851
0.004	0.5253	0.5167	0.5106	0.5199
0.0045	0.5809	0.5707	0.5635	0.5686

263 results better than *Sisyphé*, with a particular improvement at the 180° cross-section and the bedlevel erosion at both
 264 cross-sections.

265 5.2.3. Calibration study

In Section 5.2.1, we used the hydrodynamic results from *Sisyphé* to calibrate the viscosity and longitudinal slope in *Thetis* in the absence of observed data. However, Figures 11a and 11b show *Sisyphé* does not agree completely with the experimental data. Hence, to improve our model's accuracy, we re-run the calibration study using the experimental data as the 'real solution'. We seek to minimize the relative error norm at both the 90° and 180° cross-section and thus minimise

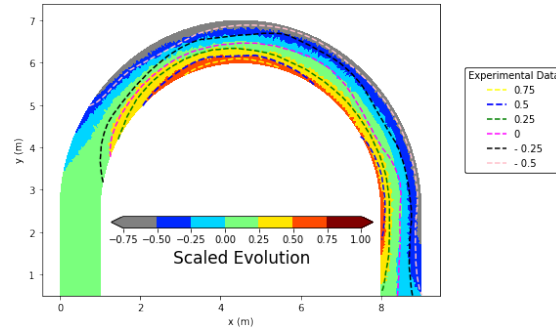
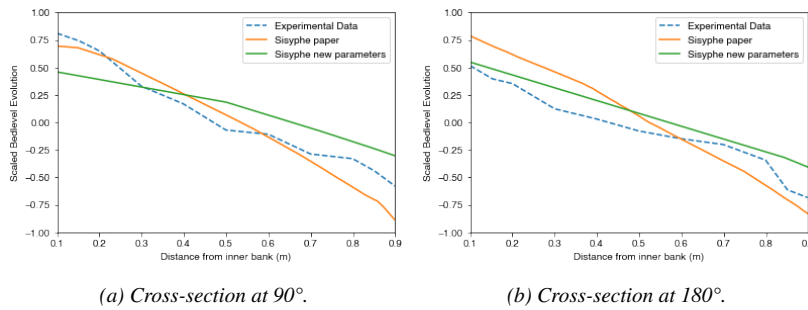
$$\frac{\|y_{90_i} - y_{90_i}^{\hat{}}\|_2}{\|y_{90_i}^{\hat{}}\|_2} + \frac{\|y_{180_i} - y_{180_i}^{\hat{}}\|_2}{\|y_{180_i}^{\hat{}}\|_2}, \quad (45)$$

where $y_{i}^{\hat{}}$ is the experimental data and y_{i} our model result. The results are summarised in Table 3 and show that a viscosity of $0.05 \text{ m}^2 \text{ s}^{-1}$ and a longitudinal slope of 0.0035 yield the best approximation to the experimental data. To ensure that by using (45) we are not merely reducing the error at one cross-section whilst allowing the error at the other cross-section to grow, we also calculate the following maximum norm

$$\max \left(\frac{\|y_{90_i} - y_{90_i}^{\hat{}}\|_2}{\|y_{90_i}^{\hat{}}\|_2}, \frac{\|y_{180_i} - y_{180_i}^{\hat{}}\|_2}{\|y_{180_i}^{\hat{}}\|_2} \right), \quad (46)$$

Table 4Maximum error norms for different values of longitudinal slope and ν ($\text{m}^2 \text{s}^{-1}$).

Slope	$\nu = 0.025$	$\nu = 0.035$	$\nu = 0.05$	$\nu = 0.075$
0.003	0.2734	0.2768	0.2834	0.3035
0.0035	0.2463	0.2534	0.2674	0.2978
0.004	0.2849	0.2644	0.2729	0.3134
0.0045	0.3332	0.3096	0.2862	0.3327

**Figure 12:** Scaled bedlevel evolution from *Thetis* with $\nu = 0.05 \text{ m}^2 \text{ s}^{-1}$, slope = 0.0035 and experimental data Yen and Lee (1995).**Figure 13:** Scaled bedlevel evolution from *Sisyphé*, Villaret et al. (2013); *Sisyphé*, present study, with $\nu = 0.05 \text{ m}^2 \text{ s}^{-1}$ and slope = 0.0035; and experimental data Yen and Lee (1995).

266 and summarise the results in Table 4. Although $\nu = 0.05 \text{ m}^2 \text{ s}^{-1}$ and a longitudinal slope of 0.0035 do not minimize
 267 Eq. (46), they result in one of the smallest maximum error norms. Comparing Figures 11 and 15, we can confirm that
 268 using these new values of ν and longitudinal slope result in a better approximation to the experimental data.

269 Using a viscosity of $0.05 \text{ m}^2 \text{ s}^{-1}$ and a longitudinal slope of 0.0035, Figure 12 shows that the scaled bedlevel
 270 evolution from *Thetis* agrees closely with the experiment, particularly at the inner bend and at the meander outflow.
 271 Comparing the experiment, *Sisyphé* (Figure 10) and our results (Figure 12), we see that *Thetis* predicts the bedlevel
 272 erosion to a greater degree of accuracy, particularly at the outer bend. Furthermore, it shows uniform erosion at the
 273 inflow bedlevel, unlike *Sisyphé* (Figure 10), although neither model predicts the inflow bedlevel particularly accurately.

274 For rigour, we run *Sisyphé* with these optimised values for viscosity and longitudinal slope. The resulting bedlevel
 275 change is shown in Figures 13a and 13b at the 90° and 180° cross-sections, respectively. There is a marginal improve-
 276 ment in the total relative error norm (45), which falls from 1.144 for the results from Villaret et al. (2013) to 1.067 for
 277 the optimised values. However, the errors of *Sisyphé* are still higher than those obtained for *Thetis*.

278 5.2.4. Sensitivity Study

279 Given *Sisyphé*'s sensitivity to Δt discussed in Section 4.2.1, we conduct a sensitivity study on Δt and Δx , main-
 280 taining a ratio between fine and coarse meshes at 2:5. We configure *Sisyphé* ourselves and use our optimised viscosity
 281 and longitudinal slope values for consistency with *Thetis*.

282 *Thetis* is insensitive to Δt (Figure 14b), whereas *Sisyphé* (Figure 14a) is sensitive to Δt , as in the migrating trench
 283 test case. Although for $\Delta t \leq 0.25 \text{ s}$ *Sisyphé*'s results are robust, for larger Δt values they are both sensitive and

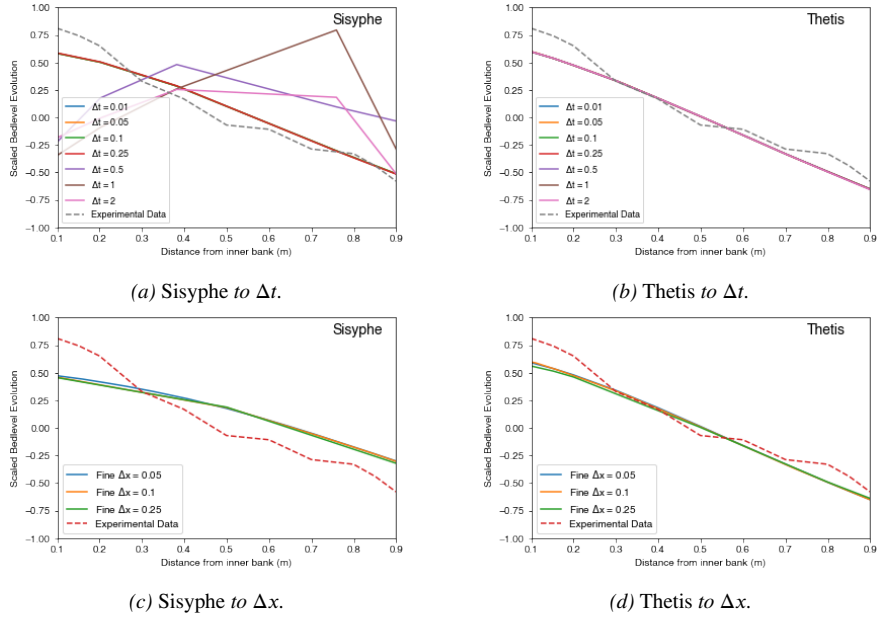


Figure 14: Sensitivity of bedlevel to Δx and Δt (90° cross-section). (*Sisyph* results, present study)

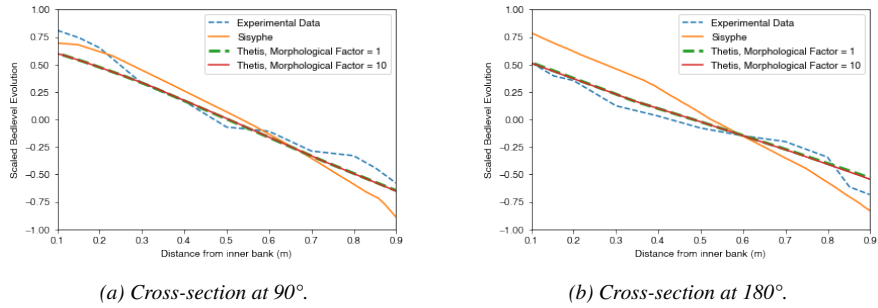


Figure 15: Scaled bedlevel evolution from *Thetis* ($\nu = 0.05 \text{ m}^2 \text{ s}^{-1}$ and slope = 0.0035) with a morphological scale factor of 1 and 10; *Sisyph*, Villaret et al. (2013); and experimental data Yen and Lee (1995).

284 inaccurate. Furthermore, for this test case, *Thetis* converges for $\Delta t < 10$ s, meaning it is much less computationally
 285 expensive than *Sisyph*, which requires $\Delta t \leq 0.25$ s.

286 Both models are relatively insensitive to the mesh step size Δx (Figures 14c and 14d). There are slight differences
 287 when a fine $\Delta x = 0.25$ m is used in both models, suggesting our fine $\Delta x = 0.1$ m is appropriate.

288 As in Section 4.2, we assess whether *Sisyph* results depend on the discretisation of the advection terms. Our
 289 preliminary results show that *Sisyph*'s sensitivity to Δt is independent of the choice of morphodynamic scheme,
 290 as indicated in the previous example. The strict Courant number stability criteria of other *Sisyph* hydrodynamic
 291 discretisations means they require small Δt to run and thus the effect is less noticeable.

292 Finally, Figures 15a and 15b provide an overview of our results and show not only that we have validated our
 293 model, but that it is more accurate than *Sisyph* for this more complex test case. Figures 15a and 15b also confirm that
 294 a morphological scale factor of 10 is appropriate with no observable difference between a morphological scale factor
 295 of 10 and 1 (*i.e.* no scaling).

296 6. Benchmarking

297 Finally, we compare the computational times and error norms of *Thetis* and *Sisyph* for both test cases discussed
 298 and summarise results in Table 5. For *Sisyph* we have chosen the most efficient matrix storage method following
 299 guidance by Lang et al. (2014). We find that for the more complex geometry of the meander, our model using the same
 300 mesh is approximately twice as accurate as *Sisyph*. For the migrating trench, we find that *Sisyph* is more accurate

Table 5

Comparison of computational time, t_s (seconds) (left) and L2 error norm to data (right) with a morphological scale factor. For the migrating trench, $\Delta t = 0.01$ s and $\Delta x = 0.2$ m in *Sisyphé* and $\Delta t = 0.6$ s and $\Delta x = 0.5$ m in *Thetis*; for the meander $\Delta t = 0.1$ s in *Sisyphé* and $\Delta t = 2$ s in *Thetis* and a fine $\Delta x = 0.1$ m in both.

Model	Morphological Factor	Migrating Trench t_s (s)	Meander t_s (s)	Migrating Trench L2 (m)	Meander L2 (m)
<i>Thetis</i>	1	66,452	17,785	0.04135	0.4752
<i>Thetis</i>	10	6590	2140	0.04084	0.4751
<i>Thetis</i>	25	2646	913	0.03920	0.4722
<i>Thetis</i>	50	1386	450	0.03666	0.4741
<i>Sisyphé</i>	1	14,113	980	0.01756	1.067

301 than our model. However, this is only true for this specific choice of mesh resolution and timestep in *Sisyphé*. As the
 302 timestep increases and the mesh becomes coarser, the accuracy of the *Sisyphé* result is found to decrease (see Figure
 303 3a and Figure 4a respectively), whereas the accuracy in our model stays broadly the same.

304 The robustness advantages observed with *Thetis*'s DG-based discretisation deliver accurate results with both larger
 305 Δt and Δx values. Without using a morphological scale factor, *Thetis* is slower, partly since on the same mesh a DG
 306 discretisation possesses significantly more degrees of freedom. However, the added robustness means we are able
 307 to readily apply a morphological scale factor to reduce computational times without compromising accuracy. Table 5
 308 presents the accuracy and efficiency results of applying a morphological scale factor. It shows that with a morphological
 309 scale factor of 50, the meander test case is two times more efficient than *Sisyphé* and the migrating trench test case is
 310 ten times more efficient, whilst retaining accuracy in the obtained results.

311 7. Conclusion

312 In this work, we have presented a new 2D depth-averaged coupled hydrodynamic and sediment transport function-
 313 ality within the finite element based coastal ocean model *Thetis*. Our model makes significant, novel contributions
 314 to the complex problem of modelling sediment transport. It is shown to be accurate, as well as more efficient and
 315 stable than other standard models. To the best of our knowledge, it is the first full morphodynamic model employing
 316 a DG based discretisation. We report on several new capabilities within *Thetis*, including bedload transport, bedlevel
 317 changes, slope effect corrections, a secondary current correction, a sediment transport source term, a velocity correc-
 318 tion factor in the sediment concentration equation, and a morphological scale factor. All these were validated using
 319 the migrating trench and meander test cases, indicating the significance of each of the additional components. The
 320 coupled and nonlinear nature of the problem makes this type of model very sensitive to parameter changes. However,
 321 *Thetis* is found to be largely insensitive to changes in timestep and mesh grid size, unlike the current state-of-the-art
 322 model *Sisyphé*, which is found to have a much larger variability, particularly with respect to the timestep in the case of
 323 the test cases considered in this work. The robustness of *Thetis* enables the application of a morphological scale factor
 324 for computational efficiency relative to existing models, whilst remaining accurate.

325 In future work, we will use our model in a coastal zone case study requiring coupled wave and current modelling.
 326 We will also use the advantages of the adjoint capabilities of *Thetis* to perform adjoint-based model calibration on our
 327 hydro-morphodynamic model, improving the accuracy of our model.

328 Acknowledgements

329 The authors thank Dr Catherine Villaret for her help in the set-up of *Sisyphé*. MCAC's work was funded through
 330 the EPSRC CDT in Mathematics for Planet Earth. AA acknowledges the support of NERC through the fellowship
 331 grant NE/R013209/2. MDP, JRP and CJC acknowledge the support of EPSRC through the grants EP/R029423/1 and
 332 EP/R007470/1.

333 Computer code availability

334 The relevant *Thetis* code for the morphodynamic model presented in this work can be found at https://github.com/mc4117/morphodynamic_model.

336 References

- 337 Amoudry, L.O., 2008. A review on coastal sediment transport modelling. Proudman Oceanographic Laboratory, Liverpool, UK.
- 338 Amoudry, L.O., Souza, A.J., 2011. Deterministic coastal morphological and sediment transport modeling: A review and discussion. *Reviews of*
339 *Geophysics* 49.
- 340 CIESIN, 2013. Low Elevation Coastal Zone (LE CZ) Urban-Rural Population and Land Area Estimates, Version 2. NASA Socioeconomic Data
341 and Applications Center (SEDAC), Palisades, New York, USA. URL: <https://doi.org/10.7927/H4MW2F2J>.
- 342 Danilov, S., 2013. Ocean modeling on unstructured meshes. *Ocean Modelling* 69, 195–210.
- 343 Dawson, C., Sun, S., Wheeler, M.F., 2004. Compatible algorithms for coupled flow and transport. *Computer Methods in Applied Mechanics and*
344 *Engineering* 193, 2565–2580.
- 345 Deltares, 2014. Delft3D-FLOW Simulation of multi-dimensional hydrodynamic flows and transport phenomena including sediments. User Manual.
346 Delft, The Netherlands. URL: https://oss.deltares.nl/documents/183920/185723/Delft3D-FLOW_User_Manual.pdf.
- 347 Englund, F., 1974. Flow and bed topography in channel beds. *Journal of the Hydraulics Division* 100.
- 348 Epshteyn, Y., Rivière, B., 2007. Estimation of penalty parameters for symmetric interior penalty Galerkin methods. *Journal of Computational and*
349 *Applied Mathematics* 206, 843–872.
- 350 Farrell, P.E., Ham, D.A., Funke, S.W., Rognes, M.E., 2013. Automated derivation of the adjoint of high-level transient finite element programs.
351 *SIAM Journal on Scientific Computing* 35, C369–C393.
- 352 Garcia, M., Parker, G., 1991. Entrainment of bed sediment into suspension. *Journal of Hydraulic Engineering* 117, 414–435.
- 353 Gerritsen, H., de Goede, E., Platzek, F., van Kester, J., Genseberger, M., Uittenbogaard, R., 2008. Validation Document Delft3D-FLOW; a software
354 system for 3D flow simulations. Technical Report. Deltares, Delft, The Netherlands.
- 355 Hervouet, J.M., 1999. TELEMAC, a hydroinformatic system. *Houille Blanche-revue Internationale De L Eau* 54, 21–28. doi:10.1051/1hb/
356 1999029.
- 357 Hervouet, J.M., 2007. *Hydrodynamics of Free Surface Flows, Modelling with the Finite-element Method*. John Wiley & Sons Ltd, West Sussex,
358 UK.
- 359 Huybrechts, N., Villaret, C., Hervouet, J.M., 2010. Comparison between 2D and 3D modelling of sediment transport: Application to the dune
360 evolution, in: *Proceedings of the 5th International Conference on fluvial Hydraulics*, Braunschweig, Germany.
- 361 Jacobs, C.T., Piggott, M.D., 2015. Firedrake-Fluids v0.1: Numerical modelling of shallow water flows using an automated solution framework.
362 *Geoscientific Model Development* 8, 533–547. doi:10.5194/gmd-8-533-2015.
- 363 Kärnä, T., Kramer, S., Mitchell, L., Ham, D., Piggott, M., Baptista, A., 2018. Thetis coastal ocean model: discontinuous Galerkin discretization for
364 the three-dimensional hydrostatic equations. *Geoscientific Model Development* 11, 4359–4382.
- 365 Kubatko, E.J., Westerink, J.J., Dawson, C., 2006. An unstructured grid morphodynamic model with a discontinuous Galerkin method for bed
366 evolution. *Ocean modelling* 15, 71–89.
- 367 Kulkarni, V., Sahoo, N., 2013. Module 5: Viscous Incompressible flow; Lecture 5 : Internal Flow – Part IV. [https://nptel.ac.in/courses/
368 101103004/module5/lec5/4.html](https://nptel.ac.in/courses/101103004/module5/lec5/4.html).
- 369 Landsberg, A., Chitchekanova, A., Lind, C., Boris, J., Young, T., 1998. *Fast3D user and programmer reference manual*. US Naval Research
370 Laboratory. Washington DC, USA.
- 371 Lang, P., Desombre, J., ATA, R., Gooury, C., Hervouet, J.M., 2014. TELEMAC-2D modelling system - User manual.
- 372 Leveque, R.J., 1996. High-resolution conservative algorithms for advection in incompressible. *SIAM Journal on Numerical Analysis* 33, 627–665.
- 373 Li, B.Q., 2006. *Discontinuous Finite Elements in Fluid Dynamics and Heat Transfer*. Springer Science & Business Media, Berlin, Germany.
- 374 McManus, T., Percival, J., Yeager, B., Barral, N., Gorman, G., Piggott, M., 2017. Moving mesh methods in Fluidity and Firedrake. Technical
375 Report July. doi:10.13140/RG.2.2.27670.24648.
- 376 Michoski, C., Dawson, C., Mirabito, C., Kubatko, E.J., Wirasaet, D., Westerink, J.J., 2013. Fully coupled methods for multiphase morphody-
377 namics. *Advances in Water Resources* 59, 95–110. URL: [http://dx.doi.org/10.1016/j.
378 advwatres.2013.05.002](http://dx.doi.org/10.1016/j.advwatres.2013.05.002).
- 379 Pan, W., Kramer, S.C., Piggott, M.D., 2019. Multi-layer non-hydrostatic free surface modelling using the discontinuous Galerkin method. *Ocean*
380 *Modelling* 134, 68–83.
- 381 Papanicolaou, A.T.N., Elhakeem, M., Krallis, G., Prakash, S., Edinger, J., 2008. Sediment transport modeling review - current and future develop-
382 ments. *Journal of Hydraulic Engineering* 134, 1–14.
- 383 Park, S.W., Ahn, J., 2019. Experimental and numerical investigations of primary flow patterns and mixing in laboratory meandering channel. *Smart*
384 *Water* 4, 4. URL: <https://doi.org/10.1186/s40713-019-0016-y>, doi:10.1186/s40713-019-0016-y.
- 385 Rathgeber, F., Ham, D.A., Mitchell, L., Lange, M., Luporini, F., McRae, A.T., Bercea, G., Markall, G., Kelly, P.H., 2017. Firedrake: automating
386 the finite element method by composing abstractions. *ACM Transactions on Mathematical Software (TOMS)* 43, 24.
- 387 Roelvink, D., Van Dongeren, A., McCall, R., Hoonhout, B., Van Rooijen, A., Van Geer, P., De Vet, L., Nederhoff, K., Quataert, E., 2015. XBeach
388 Technical Reference: Kingsday Release. Delft, The Netherlands: Deltares, Technical report .
- 389 Segur, H., 2009. Lecture 8 : The Shallow-Water Equations. Woods Hole Oceanographic Institution, Woods Hole, Massachusetts, USA.
- 390 Soulsby, R., 1997. *Dynamics of marine sands, a manual for practical applications*. Thomas Telford, London, UK.
- 391 Syvitski, J., Slingerland, R., Burgess, P., Meiburg, E., Murray, A.B., Wiberg, P., Tucker, G., Voinov, A., 2010. Morphodynamic Models: An
392 Overview. *River, Coastal and Estuarine Morphodynamics, RCEM 2009* , 3–20.
- 393 Talmon, A., Struiksma, N., Mierlo, M.V., 1995. Laboratory measurements of the direction of sediment transport on transverse alluvial-bed slopes.
394 *Journal of Hydraulic Research* 33, 495–517.
- 395 Tassi, P., Rhebergen, S., Vionnet, C., Bokhove, O., 2008. A discontinuous Galerkin finite element model for river bed evolution under shallow
396 flows. *Computer Methods in Applied Mechanics and Engineering* 197, 2930–2947.
- 397 Tassi, P., Villaret, C., 2014. *Sisyphé v6.3 User's Manual*. EDF R&D. Chatou, France.
- 398 Van Rijn, L.C., 1980. Storm surge barrier Oosterschelde-computation of siltation in dredged trenches: Semi-empirical model for the flow in dredged

399 trenches. Deltares, Delft, The Netherlands.

400 Van Rijn, L.C., 1984. Sediment Transport, Part II: Suspended Load Transport. *Journal of Hydraulic Engineering* 110, 1613–1641.

401 Villaret, C., Hervouet, J.M., Kopmann, R., Merkel, U., Davies, A.G., 2013. Morphodynamic modeling using the Telemac finite-element system.

402 *Computers & Geosciences* 53, 105–113.

403 Villaret, C., Kopmann, R., Wyncoll, D., Riehme, J., Merkel, U., Naumann, U., 2016. First-order uncertainty analysis using Algorithmic Differenti-

404 ation of morphodynamic models. *Computers & geosciences* 90, 144–151.

405 Vouriot, C.V.M., Angeloudis, A., Kramer, S.C., Piggott, M.D., 2019. Fate of large-scale vortices in idealized tidal lagoons. *Environmental Fluid*

406 *Mechanics* 19, 329–348.

407 Warner, J.C., Sherwood, C.R., Signell, R.P., Harris, C.K., Arango, H.G., 2008. Development of a three-dimensional, regional, coupled wave,

408 current, and sediment-transport model. *Computers & Geosciences* 34, 1284–1306.

409 Warren, I., Bach, H., 1992. MIKE 21: a modelling system for estuaries, coastal waters and seas. *Environmental Software* 7, 229–240.

410 Wu, W., 2007. *Computational river dynamics*. CRC Press, Boca Raton, Florida, USA.

411 Yen, C.I., Lee, K.T., 1995. Bed topography and sediment sorting in channel bend with unsteady flow. *Journal of Hydraulic Engineering* 121,

412 591–599.